Three-dimensional Modeling of the Solar Wind and Local Interstellar Medium Interaction with Pickup Ions in the Presence of Heliospheric Current Sheet

Journal of Physics: Conference Series **2742** (2024) 012010 doi:10.1088/1742-6596/2742/1/012010

Three-dimensional Modeling of the Solar Wind and Local Interstellar Medium Interaction with Pickup Ions in the Presence of Heliospheric Current Sheet

R. K. Bera

Center for Space Plasma and Aeronomic Research, The University of Alabama in Huntsville, Huntsville, AL 35899, USA

F. Fraternale

Center for Space Plasma and Aeronomic Research, The University of Alabama in Huntsville, Huntsville, AL 35899, USA

N. V. Pogorelov

Center for Space Plasma and Aeronomic Research, The University of Alabama in Huntsville, Huntsville, AL 35899, USA
Department of Space Science, The University of Alabama in Huntsville, Huntsville, AL 35899, USA

E-mail: rkb0019@uah.edu

Abstract.

Our three-dimensional, time-dependent, multi-fluid model has been used to investigate the solar wind (SW)–local interstellar medium (LISM) interaction with pickup ions (PUIs) treated as a separate fluid. A non-zero, but fixed, angle between the Sun's magnetic and rotation axis is adopted. The flow of the plasma mixture (thermal SW protons, PUIs, and electrons), is described by the system of ideal magnetohydrodynamic equations with the source terms responsible for charge exchange between ions and neutral atoms. Different populations of neutral atoms are governed by the individual sets of the Euler equations. As the standard Rankine–Hugoniot relations are not appropriate to describe the anisotropic behavior of PUIs at the termination shock, we use a kinetically-derived set of boundary conditions at it. We extend our previous work [1] and perform these new simulations on a Cartesian grid. This approach allows us to maintain a uniform grid resolution in all directions, without compromising resolution, at large distances from the Sun. The possibility of transition of the SW flow to a stochastic regime in the region between the termination shock and heliopause is further investigated.

1. Introduction

Interaction of the solar wind (SW) with the local interstellar medium (LISM) is an exciting area of space physics research which encompasses very different time and length scales. Collision of these plasma flows creates the heliosphere. The dynamical properties of the heliosphere are significantly influenced by the (time-dependent) properties of the SW and of the LISM. From the gas dynamic (or magnetohydrodynamic, MHD) perspective, the boundary between the SW

and LISM plasmas is a tangential discontinuity known as the heliopause (HP). Deceleration of the supersonic SW by the HP leads to the formation of a heliospheric termination shock (TS). Both the TS and the HP were identified in situ by the Voyager 1 (V1) and Voyager 2 (V2) spacecraft. The region between TS and HP is commonly referred to as the inner heliosheath (IHS), or simply the heliosheath. The presence of the so-called bow shock (BS) in front of the HP depends on the flow parameters in the LISM and was discussed in [2–6].

Interstellar neutral (ISN) atoms cross the HP and penetrate deeply into the heliosphere. Some of them undergo ionization through charge exchange with SW ions, solar radiation, and electron impact, giving birth to new populations of ions known as pickup ions (PUIs). Once created, PUIs respond to the motional electric field almost instantaneously and start to move outwards with the SW, acquiring its bulk speed [7]. Although their number density is low, high temperature of PUIs ($\sim 10^7$ K) makes their pressure dominant as compared both with the thermal SW and magnetic pressure in the outer heliosphere beyond ~ 20 AU. This was confirmed by Voyager 2 and New Horizons (NH) observations [8–12], and demonstrated by theoretical models and simulations [1, 13–21]. Due to the large mean free path of Coulomb collisions between PUIs and thermal SW ions, or electrons, PUIs are never in thermodynamic equilibrium with the surrounding plasma. They constitute a distinct suprathermal ion component within the SW plasma [17, 22].

Numerical simulations are essential for comprehending the three-dimensional characteristics of the SW–LISM interaction and interpreting in situ measurements by the Voyagers and NH missions, as well as remote observations made by the Interstellar Boundary Explorer (IBEX) [23–26]. It is not unusual to describe the SW–LISM interaction with multi-fluid models that are based on the combination of the ideal MHD equations and multiple sets of the Euler gas dynamics equations [1, 19, 27, 28] or kinetically [29, 30]. In recent years, significant progress has been made in incorporating PUIs into global models of the SW–LISM interaction. As was first demonstrated in [22], PUIs must be treated separately from the thermal ions. As a consequence, a number of fluid models have been developed where PUIs are treated as a separate fluid [19, 28, 31]. While PUIs away from the TS can be treated as having an isotropic distribution function, it is not so at shocks. Crossing of a collisionless shock, such as the TS, by PUIs is associated with complex kinetic processes [16, 32–37], which make the PUI distribution function in the TS vicinity highly anisotropic [16, 38, 39] and the applicability of the fluid approach questionable. While the traditional MHD Rankine—Hugoniot relations, which express the conservation of mass, momentum, energy, and magnetic flux at shocks in the mixture of charged particles, are valid at collisionless shocks on the MHD scale, it is not obvious how to derive the jumps in the PUI pressure and temperature across the TS. On the basis of extensive hybrid simulations of the PUI behavior across collisionless shocks [40], a set of boundary conditions (b.c.'s) applicable for global MHD modeling has been derived in [1].

In [1], the simulations were performed on spherical grids. The SW was assumed spherically-symmetric and the heliospheric magnetic field (HMF) was unipolar at the inner boundary of the simulation domain. Since the LISM flow is uniform and time-independent, only the stationary solutions were considered. The assumption of a unipolar HMF has been criticized earlier in [41, 42] as producing an unrealistically strong magnetic field in the IHS. In this work, we extend our model to Cartesian grids and present simulations in a more complex and computationally challenging statement, where the HMF is bipolar and a heliospheric current sheet (HCS) separates the regions of opposite polarity. These regions of positive and negative polarities are separated by the HCS and referred to as magnetic sectors. Typically, it takes a few hundred years for a steady state to be reached with our choice of initial conditions [47]. In the current simulation, the SW at the inner boundary is steady, except for the HMF polarity variations due to the Sun's rotation and a tilt between the Sun's rotation and magnetic axes. This is why, the steady state can be sought only in a statistical sense.

One advantage of Cartesian grids is that SW-LISM interaction simulations can be performed in large space domains ($\gtrsim$ 3000 AU) without compromising grid resolution at large distances. This is especially important for the SW–LISM interaction in the heliotail. Furthermore, Cartesian grids make it possible to maintain a uniform grid resolution in all directions.

Due to the non-zero tilt between the Sun's rotation and magnetic-dipole axis, the HCS naturally forms. The HCS moves with the plasma flow outward from the Sun, creating a shape that initially looks like a "ballerina skirt", although this similarity disappears with distance. It was shown in, e.g., [27, 43–45] that the HCS presence may create time-dependent features in the IHS. Moreover, it was suggested in [43] that a stochastic behavior of magnetic field can be obtained numerically when the sector regions are not resolved.

The sector width is proportional to the SW speed, so no grid is sufficient to resolve the sectors in the regions where the velocity component perpendicular to the HP is small. In the earlier simulations of this kind, PUIs were not treated as a separate fluid. Instead, an immediate assimilation of PUIs into a single Maxwellian distribution with the thermal SW was assumed. This paper supplements and extends the results of those simulations.

In Section 2, we briefly describe our physical and mathematical models. The simulation setup and boundary conditions are discussed in Section 3. The implementation of b.c's for the PUIs crossing the TS is described in Section 4. The simulation results are presented in Section 5, which is followed by the conclusions in Section 6.

2. Physical Model

We build our model on the multi-fluid approach described in [19, 46, 47] and further elaborated in [1]. We solve a system of equations governing the flow of the whole mixture of charged particles, neutral atoms, and PUIs. The plasma mixture consists of three co-moving populations of charged particles: thermal protons, electrons, and PUIs. This flow is described by the ideal MHD equations with the source terms responsible for charge exchange. We also distinguish three populations of neutral hydrogen (H) atoms: population 1 represents H atoms of interstellar origin, while populations 2 and 3 are the neutral atoms born by charge exchange in the IHS and in the supersonic SW, respectively. Each of these atom populations originates from thermodynamically distinct regions of the heliosphere (we call the Regions 1, 2, and 3), thus necessitating the use of separate sets of Euler equations to describe their behavior. PUIs are treated as a separate co-moving fluid by solving the corresponding continuity and pressure equations. The complete system of equations is given in [1, 19].

The analytical expressions for the source terms are derived assuming Maxwellian distributions for ions and neutral atoms.

The electron density is calculated assuming the quasi-neutrality condition, $n_\mathrm{e} = n_\mathrm{p,th} + n_\mathrm{PUI} = n$, where n_e, $n_\mathrm{p,th}$, and n_PUI are the electron, thermal proton, and PUI number densities, respectively. The electron temperature is assumed to be equal to the temperature of thermal protons, $T_\mathrm{e} = T_\mathrm{p,th}$. The thermal pressure of each species is determined using the equation of state, $p_s = n_s k_\mathrm{B} T_s$, where p_s, n_s and T_s are the pressure, number density, and temperature of species s, and k_B is the Boltzmann constant. There is no need to solve separate equations for the thermal protons. Their properties can be derived from those of the mixture and PUIs.

A significant fraction of the thermal proton heating in the distant SW is caused by PUI-generated turbulence [31, 33, 48–50]. Here we adopt a simplified approach [1], where the source term in the PUI pressure equation is decreased by 5%. This automatically transfers some amount of energy from PUIs to thermal protons in our model. The fraction of energy to be transferred is adjusted to make the temperature of the thermal SW closer to that in V2 data. This modification of the source term is done only in the supersonic SW.

In addition to Eqs. (1)–(9) from [1], we solve three level-set equations, as described in [45]. The first level set is used to correctly identify the position of the HP by tracking the time

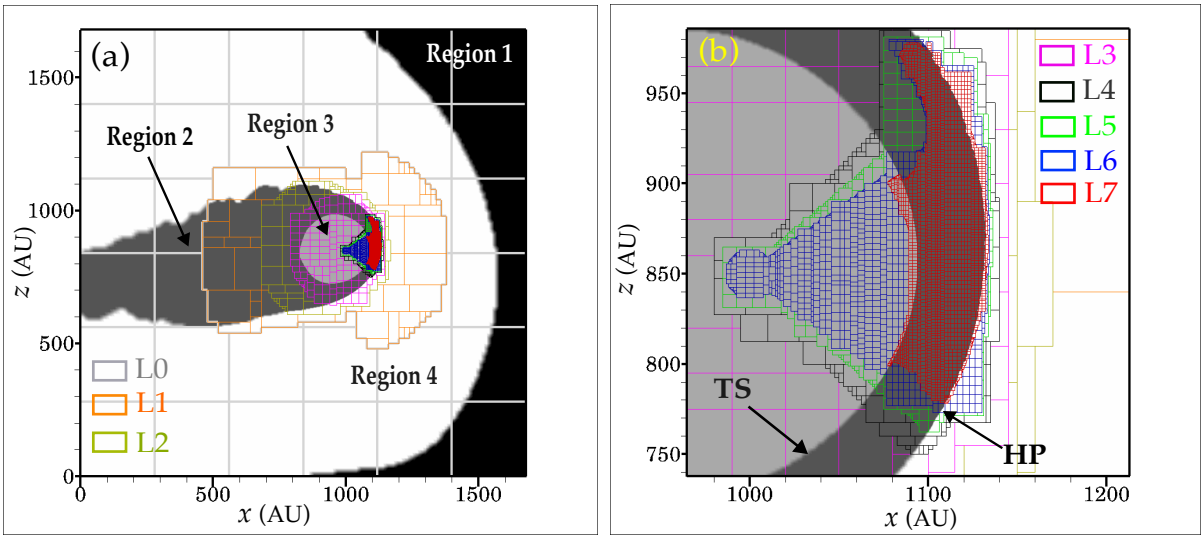

Figure 1. The numerical grid used in our simulation. The left panel shows the grid patches corresponding to all seven levels of refinements (L0-L7, color-coded) in the meridional plane. The right panel shows a zoomed view of the most refined regions.

evolution of its surface starting from the initial position at time $t = 0$. The other two level-set equations are introduced to identify the HCS and the boundary of the region covered by the magnetic field sectors.

3. Simulation Setup and Boundary Conditions

We solve the system of equations using the Multi-Scale Fluid-Kinetic Simulation Suite (MS-FLUKSS), which takes advantage of the Chombo adaptive mesh refinement (AMR) framework for efficient data choreography [1, 19, 21, 23, 29, 45, 47, 51, 52]. The simulation is performed on a Cartesian grid (x, y, z). The simulation domain is a cube with each side equal to 1680 AU. The z-axis is set to be parallel to the Sun's rotation axis. The x-axis belongs to the plane containing the z-axis and the velocity vector in the unperturbed LISM, $\mathbf{V}_{\rm LISM}$, and is oriented upstream into the LISM. The y-axis completes the right coordinate system. The Sun's position is at $(x_S, y_S, z_S) = (1000, 850, 850)$ AU. The objective of this paper is to test the model and assess the performance of our new code while addressing a challenging problem previously analyzed in [53], i.e., the SW–LISM interaction in the presence of an HCS under the assumption of a fixed tilt of the Sun's magnetic axis to its rotation axis. This is a computationally challenging problem. Due to the deceleration of the SW flow initially at the TS and further by the HP, the sector width decreases substantially approaching zero at the HP (see the discussion in Section 5). Therefore, from the perspective of global MHD simulations, it is practically impossible to resolve the sector structure in the HP vicinity.

The base grid size in our simulations is $\Delta x = \Delta y = \Delta z = 10$ AU. Seven levels of refinements with a refinement ratio equal to 2 at each level are applied. This creates the finest resolution of ≈ 0.07 AU cubed. Figure 1 shows the boundary of grid patches corresponding to the different levels as seen in the meridional plane (x-z plane), labeled from L0 to L7. The finest level (L7) is used in the IHS to cover the latitudinal extent of the sector region (the region containing the HCS) ($\pm 60°$ from the equatorial plane). In the azimuthal direction, the grid extends from $-15°$ to $35°$ from the x-axis to cover a broad region the direction towards the SW stagnation point. L7 starts in the supersonic SW a few AU ahead of the TS and extends to a few AU into the LISM, to cover the HP. The total number of cells is approximately 3×10^9.

Table 1 summarizes the inner and outer boundary conditions used in our simulations. The

Table 1. The boundary conditions used at 1 AU and at outer boundary.

Parameters at 1 AU	Value
Thermal proton density	9 cm^{-3}
SW speed	420 km s^{-1}
SW temperature	90000 K
Radial HMF component	39 μG
PUI density at 10 AU	1.5×10^{-3} cm^{-3}
PUI temperature at 10 AU	3.36×10^{6} K
LISM parameters	**Value**
Proton density	0.054 cm^{-3}
Flow speed	25.4 km s^{-1}
Plasma temperature	7500 K
ISMF strength	3.5 μG
Neutral H density	0.2 cm^{-3}
Velocity direction (HAE-J2000)	$(255°.7, 5°.1)$
ISMF (HAE-J2000)	$(224°.46, 36°.61)$

physical boundary conditions are enforced at $R_0 = 10$ AU. It is assumed that the SW is radial and its scalar properties are spherically symmetric at this boundary. Technically speaking, there is no mathematical inner boundary in the Cartesian simulation domain, i.e., we have the computational cells at distances smaller than 10 AU, but the quantities in those cells are substituted with the analytical, Parker's solution. However, only the ghost cells adjacent to the physical boundary are used. For the neutral fluids, there is no physical inner boundary

While the SW properties are known at the Earth orbit ($R = 1$ AU), we use the polytropic expressions to translate them from 1 AU to 10 AU. The choice of SW properties at 1 AU is based on the averaged OMNI data for the period from 2012 to 2022. The number density, velocity, and temperature of the SW at the inner boundary are stationary. The magnetic field vector at the inner boundary is assumed to be a Parker spiral [54]. The variation of the HCS location at the inner boundary, as a function of time due to the solar rotation with a period of 25 days, is given in [55]. As a consequence, the HMF strength, $\mathbf{B}$, and the boundary between the regions of its opposite polarity, become functions of time. The PUI properties at 10 AU are specified based on the NH observations [12]. The ghost cells beyond the outer boundary are filled with the properties of the undisturbed LISM, characterized by time-independent values based on recently accepted parameters. Numerical fluxes through the outer boundary are obtained with the method described in [56, 57].

4. Treatment of PUIs at the Termination Shock

To describe the behavior of PUIs at the TS, we employ the shock relations recently described in [1]. They are obtained by summarizing the hybrid simulations from [40] in such a way that the *isotropic* temperature of PUIs well behind the TS is obtained in terms of the three local upstream shock parameters, i.e., the Alfvénic Mach number (M_{A}), plasma beta (β), and the angle between the shock normal and the upstream magnetic field (θ_{Bn}). The shock normal is calculated using the formulae given by [58]. Note that the upstream shock parameters are readily available in our global model of the plasma mixture. The idea is to substitute the solution to the PUI pressure equation behind the shock with the PUI pressure derived from the kinetic (hybrid) simulations. It is worth noting that we do not modify the plasma mixture explicitly, therefore it continues to satisfy the MHD conservation laws. A detailed derivation of the b.c.'s from the hybrid simulation results and their implementation in MS-FLUKSS are discussed in [1].

The application of such b.c.'s requires identification of the cells adjacent to the TS, both upstream and downstream. The algorithm designed for this purpose on spherical grids is developed in [1]. Then, it is relatively straightforward to choose the downstream and upstream cells for a given shock-containing cell. This is illustrated in Figure 1(a), where the shock-containing cells are colored red, with the upstream and downstream cells being of blue and green color, respectively. We label the shock cell and its corresponding upstream and downstream cells with S, U, and D. The shock has necessarily a numerical structure, with the typical thickness of a few cells along the normal direction. A shock cell, S, is identified as a cell that meets the following two simultaneous conditions: (i) it belongs in region 2, and (ii) it shares at least one neighboring cell in region 3. We found that the results are sensitive to the choice of the upstream cell and that it is essential to choose upstream cells carefully. Specifically, it is crucial to avoid (i) selecting a cell within the shock structure (indicated by the layer of white cells between the red and blue cells in panel (a)) and (ii) selecting a cell too far upstream because of the SW changing with the heliocentric distance. The second issue is partially mitigated when the grid resolution is very high.

The algorithm for selecting the upstream and downstream cells becomes more complicated for Cartesian grids. We illustrate the newly developed procedure in the right panel of Figure 2. The selection of shock cells (red cells in the figure) is based on the previously described criteria, i.e., we identify all cells that have at least one side adjacent to Region 3 while belonging to Region 2. For each of these cells, we then identify one appropriate upstream cell (blue) and one downstream cell (green). The coordinates of an ideal upstream point are obtained analytically using the direction of the flow (or the radial direction) and by setting a distance 2δ from the shock cell. Afterward, the cell closest to this point can be immediately found. For the reasons outlined above, we set $\delta = 1.2\Delta x$. The same procedure is used to select the downstream cell, in which the PUI pressure is modified, but the distance is set equal to δ in this case.

However, after this procedure is applied to all red cells, there remain a few more downstream cells that require modifications (yellow cells in the figure). We identify these cells and modify the PUI pressure in them by applying an appropriate interpolation procedure. Otherwise, the PUI pressure may become excessively low at these cells, creating spurious fluctuations in the heliosheath.

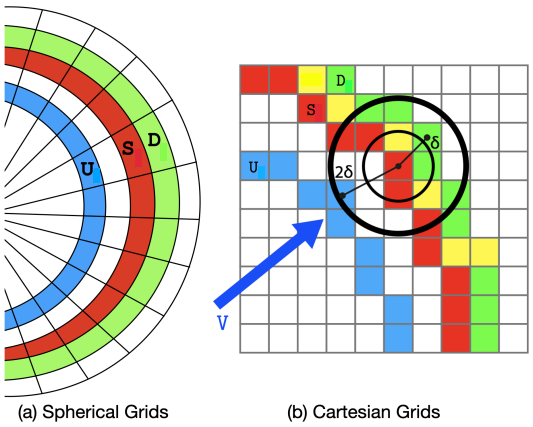

Figure 2. Schematic for the implementation of shock b.c.'s for PUIs in spherical and Cartesian grids.

5. Numerical results

We present solutions that have evolved beyond 300 years from the initial condition. Figure 3(a) shows the distribution of PUI pressure ($p_{\rm PUI}$) in the meridional plane. To demonstrate the effect of the b.c.'s for PUIs at the TS, in Fig. 3(b) we compare the PUI pressure distributions along the x-axis obtained with the application of our b.c.'s (red curve) and without them (blue curve). Hereinafter these simulations as labeled as "TS-BC" and "no TS-BC." It is seen that the PUI pressure increases by approximately $40-50\%$ behind the shock when the TS-BC approach is used. It can also be seen that the IHS becomes narrower by a few AU. This is associated with cooling of the IHS plasma caused by the enhanced charge exchange. A detailed discussion of this effect can be found in [1]. Our simulation clearly shows the presence of the HCS, which

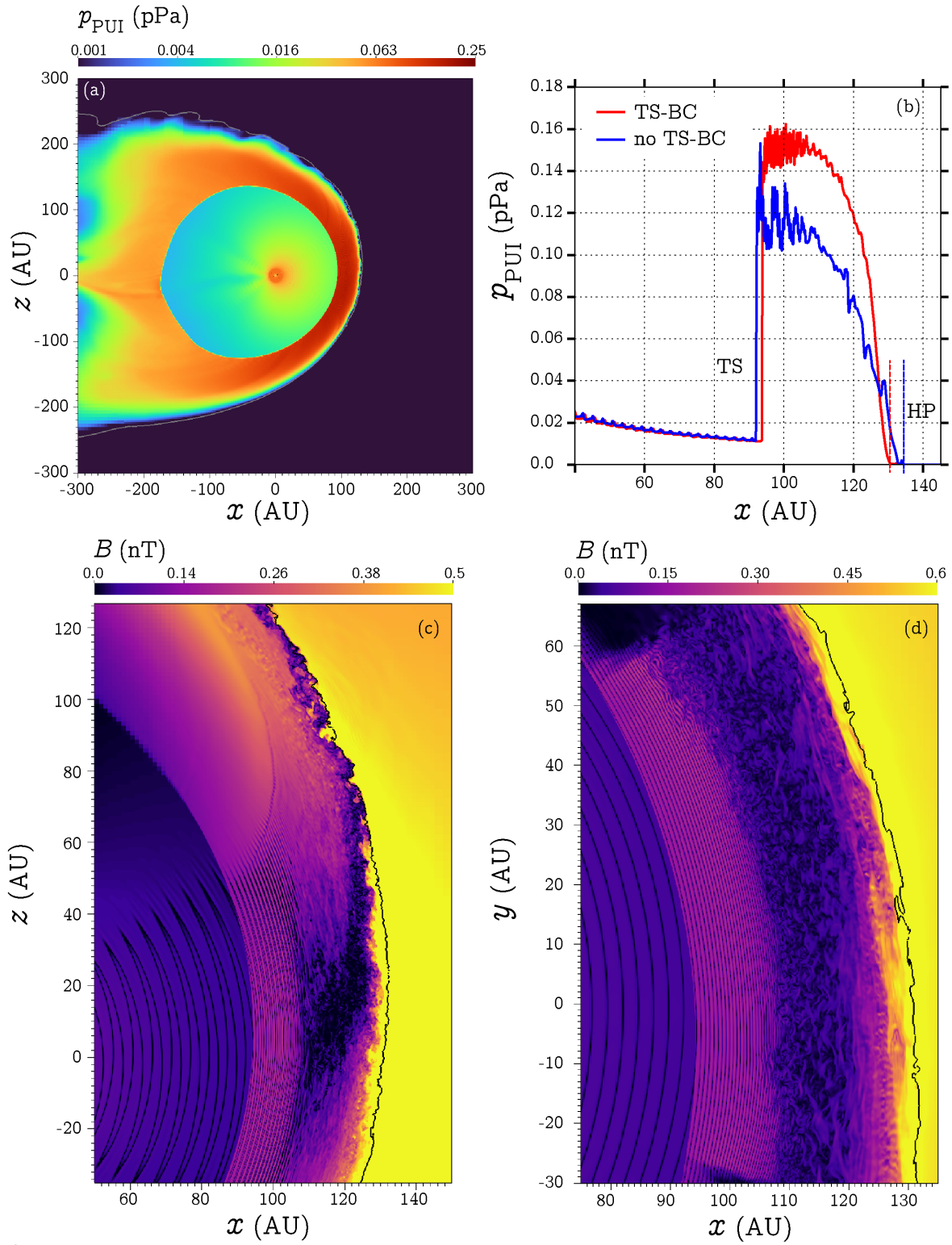

Figure 3. (Panel a) PUI pressure in the meridional plane with the shock b.c.'s; (panels b and c) PUI pressure along x-axis in the simulation with our b.c.'s at the TS (red curve) and without them (blue curve); and (panels c and d) magnetic field strength in the meridional and equatorial planes. The position of the HP is indicated by the white contour line in panel (a) and by the black contour lines in panels (c) and (d). Note that the grid boundaries can be seen in the equatorial plane.

is also seen in the PUI distributions. In particular, in the regions of well-resolved magnetic sectors, the PUI pressure increases inside the HCS, which results in periodic variations of about 15-20%. This occurs because of energy conservation, which is ensured by the MHD statement of the problem. Decreases in magnetic pressure are accompanied by increases in the thermal

pressure of plasma, and vice versa. The numerical HCS structure inevitably contains a point where $B = 0$. Indeed, some, but not all, current sheet crossings identified by Voyagers exhibited small (below 0.02 nT) values of B. A typical width of these sheets was observed to be of the order of ~ 15 PUI gyroscales ($\sim 5 \times 10^{-3}$ AU) [59–61]. This is way below our grid resolution. It is to be reminded that such a regular sector structure does not exist in the realistic SW. It was shown in [62] that fewer HCS crossings were observed by V2 in the IHS than it was expected on the basis of OMNI data at 1 AU.

Both solutions exhibit a wave-like behavior, but they occur on different scales (Figure 3b). The small-scale oscillations present in both curves are attributed to the physical presence of the HCS. However, it's noteworthy that the simulation without the TS-BC approach (blue curve) also exhibits larger-scale oscillations, which are identified as numerical artifacts. They arise because of the differences in numerical smearing of the plasma mixture and PUI pressure profiles across the TS. The smearing of the latter is stronger because the PUI pressure equation is being solved instead of the MHD equations in the conservation-law form applied to the mixture. Consequently, the actual numerical structure of the TS is wider for PUIs as compared with the plasma mixture. As they both are further used to calculate the analytic source terms, inappropriate, and inaccurate, values occasionally occur inside numerical shock structures. They, in turn, affect the source terms and eventually the PUI pressure. These issues are absent when the TS-BC approach is used.

The bottom panels of Figure 3 show the distributions of magnetic field magnitude in the meridional (panel c) and equatorial (panel d) planes. As in [53] (see Figure 14 therein), the sector region of the IHS gets compressed with the distance from the TS and bends as a whole following the plasma flow. Similarly to [53], a transition to turbulence, or stochasticity, is also seen in the IHS. This happens when the sectors become sufficiently compressed to trigger a tearing mode instability and consequent (numerical) magnetic reconnection. This behavior is in contrast with the solution presented in [44].

It is clear that this "turbulence" is underresolved and numerically dissipates on the grid. In the actual SW, the MHD turbulence cascade proceeds down to scales as small as a few thousand km [26, 63] and filamentary structures are created at the reconnection sites. These filamentary structures are roughly aligned with the z-axis. They evolve towards isotropic eddies, which eventually become elongated azimuthally as they are advected outward.

The distributions shown in Figure 3 are qualitatively similar to those obtained in [53]. The differences are due to the presence of PUIs treated as a separate fluid and may be affected by the differences in boundary conditions. In particular, [53] shows the the streamlines carrying magnetic field polarity on the unipolar region of the southern hemisphere turn upward into the northern hemisphere creating a unipolar "magnetic barrier" on the inner side of the HP surface. It is not entirely clear that this will ultimately happen in our solution if the SW stagnation point remains in the sector region, which would result in a layer of "turbulent" magnetic field spreading over the entire HP. Moreover, the wavenumber anisotropy of turbulence seems to differ from the previous calculations made on a spherical grid with the high computational cell aspect ratio.

6. Conclusions

We have extended the model presented in [1] to Cartesian grids. The new model utilizes a multi-fluid description of three-dimensional SW–LISM interaction with PUIs treated as a separate fluid and uses kinetically derived b.c.'s at the TS to describe their behavior. The model was used to investigate the SW-LISM interaction in the presence of a global HCS separating regions of opposite magnetic field polarity. The HCS presence affects the PUI properties by imposing oscillations on the length scale corresponding to the sector width. With a resolution of ≈ 0.07 AU in IHS, we were able to qualitatively reproduce the transition to turbulence in the IHS, as

was first described in [53]. However, a number of noticeable differences between these two results were identified. The presence of MHD turbulence in the IHS and its impact on the properties of the heliosphere require further detailed investigation. It will be presented elsewhere. The new model is capable of investigating time-dependent SW–LISM interactions. In our future publications, we will further investigate the solar-cycle effects on the SW–LISM interaction. Data-driven simulations, similar to those in [64], are expected to be performed.

7. Acknowledgements

This work is supported by NASA grants 80NSSC18K1212, 80NSSC18K1649, 80NSSC24K0267, and NSF-BSF grants 2010450, 2010144 and 2019744. The authors acknowledge the Texas Advanced Computing Center (TACC) at The University of Texas at Austin for providing HPC resources on Frontera supported by NSF award CISE-OAC-2031611. Supercomputer time allocations were also provided by NASA High-End Computing Program award SMD-17-1537. FF and NP acknowledge support from the International Space Science Institute (ISSI) in Bern, through ISSI International Team project #574 "Shocks, Waves, Turbulence, and Suprathermal Electrons in the Very Local Interstellar Medium".

References

[1] Bera R K, Fraternale F, Pogorelov N V, Roytershteyn V, Gedalin M, McComas D J and Zank G P 2023 *ApJ* **954** 147
[2] Florinski V, Pogorelov N V, Zank G P, Wood B E and Cox D P 2004 *ApJ* **604** 700
[3] Pogorelov N V, Heerikhuisen J, Zank G P, Borovikov S N, Frisch P C and McComas D J 2011 *ApJ* **742** 104
[4] McComas D J, et al. 2012 **336** 1291–1293
[5] Zank G P, Heerikhuisen J, Pogorelov N V, Zirnstein E, Wood B E and McComas D J 2013 *ApJ* **763**
[6] Pogorelov N V, Heerikhuisen J, Roytershteyn V, Burlaga L F, Gurnett D A and Kurth W S 2017 *ApJ* **845** 9
[7] Parker E 1965 **13** 9–49
[8] Richardson J D, Paularena K I, Lazarus A J and Belcher J W 1995 *GRL* **22** 1469–1472
[9] Richardson J D and Smith C W 2003 *GRL* **30** 10
[10] Decker R B, Krimigis S M, Roelof E C, Hill M E, Armstrong T P, Gloeckler G, Hamilton D C and Lanzerotti L J 2008 *Nat* **454** 67–70
[11] McComas D J, et al. 2017 *ApJS* **233** 8
[12] McComas D J, et al. 2021 *ApJS* **254** 19
[13] Wallis M 1971 *NPhS* **233** 23–25
[14] Vasyliunas V M and Siscoe G L 1976 *JGRA* **81** 1247–1252
[15] Malama Y G, Izmodenov V V and Chalov S V 2006 *A&A* **445** 693–701
[16] Zank G P, Pauls H L, Cairns I H and Webb G M 1996 *JGRA* **101** 457–477
[17] Zank G P, Hunana P, Mostafavi P and Goldstein M L 2014 *ApJ* **797** 87
[18] Zank G P, Adhikari L, Zhao L L, Mostafavi P, Zirnstein E J and McComas D J 2018 *ApJ* **869** 23
[19] Pogorelov N V, Bedford M C, Kryukov I A and Zank G P 2016 *JPhCS* **767**
[20] Kim T K, Pogorelov N V, Zank G P, Elliott H A and McComas D J 2016 *ApJL* **832** 72
[21] Kim T, Kryukov I, Pogorelov N, Elliott H and Zank G P 2018 *ESSOAr* 1
[22] Isenberg P A 1986 *JGRA* **91** 9965–9972
[23] Pogorelov N V, et al. 2017 *SSRv* **212** 193–248
[24] Kleimann J, et al. 2022 *SSRv* **218** 36
[25] Sokół J M, et al. 2022 *SSRv* **218**
[26] Fraternale F, et al. 2022 *SSRv* **218** 50
[27] Pogorelov N V, Borovikov S N, Zank G P and Ogino T 2009 *ApJ* **696** 1478
[28] Opher M, Loeb A, Drake J and Toth G 2020 *NatAs* **4** 675–683
[29] Heerikhuisen J, Zirnstein E J, Pogorelov N V, Zank G P and Desai M 2019 *ApJ* **874** 76
[30] Fraternale F, Pogorelov N V and Bera R K 2023 *ApJ* **946** 97
[31] Usmanov A V, Goldstein M L and Matthaeus W H 2016 *ApJ* **820** 17
[32] Gedalin M, Balikhin M and Krasnosselskikh V 1995 *AdSpR* **15**(8-9)
[33] Richardson J D, Kasper J C, Wang C, Belcher J W and Lazarus A J 2008 *Nat* **454** 63–66
[34] Gedalin M, Pogorelov N V and Roytershteyn V 2021 *ApJ* **916** 57
[35] Zank G P, Heerikhuisen J, Pogorelov N V, Burrows R and McComas D 2010 *ApJ* **708** 1092–1106

[36] Chalov S V and Fahr H J 2000 *A&A* **360** 381–390
[37] Giacalone J, Nakanotani M, Zank G P, Kòta J, Opher M and Richardson J D 2021 *ApJ* **911** 27
[38] Chalov S V, Malama Y G, Alexashov D B and Izmodenov V V 2015 *MNRAS* **455** 431
[39] Gedalin M, Pogorelov N V and Roytershteyn V 2021 *ApJ* **910** 107
[40] Gedalin M, Roytershteyn V and Pogorelov N V 2023 *ApJ* **945** 50
[41] Pogorelov N V, et al. 2017 *SSRv* **212** 193–248
[42] Pogorelov N V, Fraternale F, Kim T K, Burlaga L F and Gurnett D A 2021 *ApJ* **917** L20
[43] Pogorelov N V, Borovikov S N, Bedford M C, Heerikhuisen J, Kim T K, Kryukov I A and Zank G P 2013 *Numerical modeling of space plasma flows: Astronum-2012* vol 474 ed Pogorelov N V, Audit E and Zank G P 165
[44] Opher M, Drake J F, Schoeffler K M, Richardson J D, Decker R B and Toth G 2011 *ApJ* **734** 71
[45] Borovikov S N, Pogorelov N V, Burlaga L F and Richardson J D 2011 *ApJL* **728** L21
[46] Pauls H L and Zank G P 1997 *JGRA* **102** 19779
[47] Pogorelov N V, Zank G P and Ogino T 2006 *ApJ* **644** 1299
[48] Williams L L, Zank G P and Matthaeus W H 1995 *JGRA* **100** 17059
[49] Matthaeus W H, Zank G P, Oughton S, Mullan D J and Dmitruk P 1999 *ApJ* **523** L93
[50] Isenberg P A, Smith C W, Matthaeus W H and Richardson J D 2010 *ApJ* **719** 716
[51] Pogorelov N V, Borovikov S, Heerikhuisen J, Kim T, Kryukov I and Zank G P 2014 *Proc. 2014 Ann. Conf. on Extreme Science and Engineering Discovery Environment* XSEDE'14
[52] Kryukov I A, Pogorelov N V, Zank G P and Borovikov S N 2012 *American Institute of Physics Conference Series* (*American Institute of Physics Conference Series* vol 1436) ed Heerikhuisen J, Li G, Pogorelov N and Zank G 48
[53] Pogorelov N V, Suess S T, Borovikov S N, Ebert R W, McComas D J and Zank G P 2013 *ApJ* **772** 2
[54] Parker E N 1961 *ApJ* **134** 20
[55] Pogorelov N V, Stone E C, Florinski V and Zank G P 2007 *ApJ* **668** 611
[56] Pogorelov N V and Semenov A Y 1997 *A&A* **321** 330
[57] Kulikovskii A G, Pogorelov N V and Semenov A Y 2000 *Mathematical Aspects of Numerical Solution of Hyperbolic Systems* Monographs and Surveys in Pure and Applied Mathematics (Chapman & Hall/CRC)
[58] Abraham-Shrauner B 1972 *JGRA* **77** 736
[59] Burlaga L F and Ness N F 2011 *JGRA* **116** A05102
[60] Burlaga L F and Ness N F 2014 *ApJ* **784** 146
[61] Burlaga L F, Ness N F and Richardson J D 2017 *ApJ* **841** 47
[62] Richardson J D, Burlaga L F, Drake J F, Hill M E and Opher M 2016 *ApJ* **831** 115
[63] Fraternale F, Pogorelov N V, Richardson J D and Tordella D 2019 *ApJ* **872** 40
[64] Kim T K, Pogorelov N V and Burlaga L F 2017 *ApJL* **843** L32